Lawrence Berkeley National Laboratory
Molecular Biophys & Integ Bi

Title

Insights into the Li Diffusion Dynamics and Nanostructuring of H2Ti12O25 To Enhance Its Li Storage Performance

Permalink

https://escholarship.org/uc/item/7bg4c373

Journal

ACS Applied Materials & Interfaces, 8(19)

ISSN

1944-8244

Authors

Park, Soomin
Yoo, Young Geun
Nam, Inho
et al.

Publication Date

2016-05-18

DOI

10.1021/acsami.6b02842

Peer reviewed

Insights into the Li Diffusion Dynamics and Nanostructuring of H₂Ti₁₂O₂₅ To Enhance Its Li Storage Performance

Soomin Park,[†,§] Young Geun Yoo,[†,§] Inho Nam,[†] Seongjun Bae,[†] Jongseok Park,[†] Jeong Woo Han,[‡] and Jongheop Yi[*,†]

[†]World Class University (WCU) Program of Chemical Convergence for Energy & Environment, School of Chemical and Biological Engineering, Institute of Chemical Processes, Seoul National University, Seoul 151-742, Republic of Korea

[‡]Department of Chemical Engineering, University of Seoul, Seoul 130-743, Republic of Korea

Ⓢ *Supporting Information*

ABSTRACT: Dodecatitanate H₂Ti₁₂O₂₅ crystal has a condensed layered structure and exhibits noteworthy Li storage performance that makes it an anode material with great potential for use in Li-ion batteries. However, an unknown Li diffusion mechanism and a sluggish level of Li dynamics through elongated diffusion paths inside this crystal has impeded any forward development in resolving its limited rate capability and cyclic stability. In this study, we investigated the Li diffusion dynamics inside the H₂Ti₁₂O₂₅ crystal that play an essential role in Li storage performance. A study of density functional theory combined with experimental evaluation confirmed a strong dependence of Li storage performance on its diffusion. In addition, a nanostructured H₂Ti₁₂O₂₅ containing a bundle of nanorods is developed via the introduction of a kinetic gap during the structural transformation, which conferred a significantly shortened diffusion time/length for Li in H₂Ti₁₂O₂₅. The nanostructured H₂Ti₁₂O₂₅ has high specific capacity (~230 mAh g⁻¹) and exhibits enhanced cyclic stability and rate capability compared with conventional bulky H₂Ti₁₂O₂₅. The H₂Ti₁₂O₂₅ proposed in this study has high potential for use as an anode material with excellent safety and stability.

KEYWORDS: *H₂Ti₁₂O₂₅, Li-ion battery, anode, Li diffusivity, rate capability*
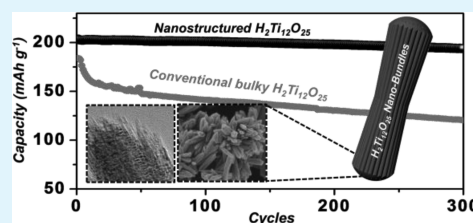
■ INTRODUCTION

Because of the rapidly expanding demand for Li-ion batteries (LIBs) for use in large-scale electronics (robots, electric vehicles, and smart grid systems), safety problems related to their size have also become a more significant factor.[1,2] It is important to note that the problems involved with the formation of a solid electrolyte interface (SEI) and with thermal susceptibility have caused major obstacles in ensuring the safety of LIBs. To address these SEI-related issues, many attempts have been made to develop high-voltage anode materials that are operable at more than 1.0 V (vs Li/Li⁺).[3−6]

The family of titanium-based oxides has been the most intensively studied high-voltage anode material for use in LIBs. In essence, titanium-based oxide materials have a high degree of chemical/physical stability and cost-effectiveness, and they are thermally stable with low exothermic behavior. In addition, the crystal polymorphism of the materials provides open access to the construction of desired Li host nanocrystals based on a structure−property relationship. Until now, spinel Li₄Ti₅O₁₂ (LTO) and TiO₂ polymorphs have been representative high-voltage materials due to their well-established Li dynamics.[7−12]

Dodecatitanate H₂Ti₁₂O₂₅ (HTO) is an intermediate structure formed by topotactic dehydration during H₂Ti₃O₅ → TiO₂ rearrangement.[13] The condensed layered structure of HTO with its atomic-scaled tunnel-like morphology is capable of providing a sufficient number of insertion sites for Li storage

via a two-phase reaction. As a result, HTO exhibits a reversible capacity of more than 200 mAh g⁻¹ with a flat voltage plateau at approximately 1.55 V (vs. Li/Li⁺),[14,15] which indicates that HTO has noticeable advantages as an advanced high-voltage anode material for LIBs (Figure S1). Despite its potential, HTO has a limited capacity at high current density and a continued fading of capacity over repeated charge−discharge cycles, which is supposedly related to the veiled Li dynamics in HTO. For these reasons, HTO materials have not been widely used, and the underlying Li storage mechanism remains unexplored.

To elucidate and overcome the problematic electrochemical performance of HTO, this work describes two achievements. (1) The Li storage reaction inside the HTO crystal was examined from a kinetic perspective. Specifically, the characteristics of Li diffusion inside the HTO crystal were identified and quantified by ab initio calculations using density functional theory (DFT). These calculations and experimental data confirm a strong dependence of Li storage performance on Li diffusion within the crystal. (2) On the basis of an analytical understanding, we proposed the use of a nanostructured HTO, which would confer a significantly shortened diffusion time/
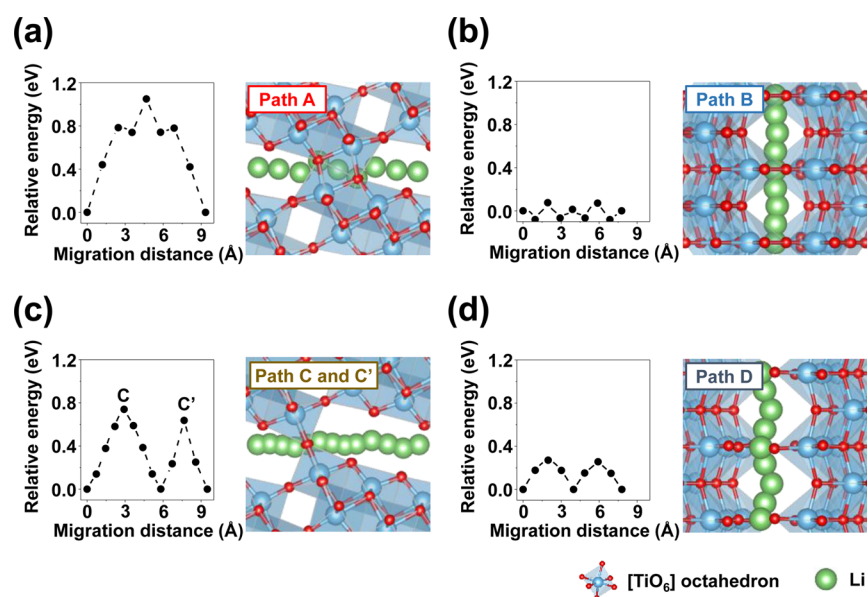
Figure 1. DFT-calculated relative energies along the different migration paths that exist inside the HTO crystal and the corresponding crystal structure of Li-inserted HTO near each path. (a, c) Paths A and C represent Li migration along the a-direction. (b, d) Paths B and D correspond to the movement of Li through channels in the c-direction.

length of Li in $H_2Ti_{12}O_{25}$. The nanostructured $H_2Ti_{12}O_{25}$ showed enhancements in specific capacity, cyclic stability, and rate capability when compared with the corresponding values for conventional bulky $H_2Ti_{12}O_{25}$.

■ EXPERIMENTAL SECTION

Preparation and Characterization of HTO. HTO samples were sequentially synthesized via the recrystallization of TiO_2 to $Na_2Ti_3O_7$, Na^+/H^+ ion exchange, and dehydration/condensation reactions upon heat treatment (Figure S2). First, $Na_2Ti_3O_7$ samples were prepared via solid-state heat treatment using three types of TiO_2 nanoparticles with anatase (COTIOX KA-100, Cosmo Chemical), rutile (Titanium(IV) oxide, rutile, Aldrich), and anatase/rutile mixed phases (Aeroxide TiO_2 P 25, Evonik). Sodium carbonate (≥99.0%, Sigma-Aldrich) and TiO_2 particles were mixed in a 1:3 molar ratio (0.53 g of Na_2CO_3 + 1.2 g of TiO_2). The finely ground mixture was heat-treated under air at 800 °C for 20 h. After being cooled to room temperature, the sample was ground and heat-treated again under the same conditions. For the Na^+/H^+ ion exchange, 0.75 g of the resultant $Na_2Ti_3O_7$ was then placed in 200 mL of 1.0 M HCl with deionized water and stirring at 60 °C for 5 days. The reaction mixture was centrifuged and washed twice with water and ethanol. The product was dried at 70 °C to obtain the $H_2Ti_3O_7$. The final HTO was obtained after heat treatment of the $H_2Ti_3O_7$ at 260 °C for 5 h under air. The morphologies of the samples were examined by transmission electron microscopy (TEM, JEOL, JEM-3010) and scanning electron microscopy (SEM, Carl Zeiss, SUPRA 55VP). An X-ray diffractometer (XRD, Rigaku, D/max-2200) was utilized to investigate the crystalline structure of the samples.

Electrochemical Measurements. Electrochemical experiments were performed using a conventional coin cell (CR2032) assembled in an Ar-filled glovebox. Lithium foil and microporous polypropylenes were used as the counter electrode and separator, respectively. The working electrodes were fabricated using 80% w/w of the HTO, 10% w/w conductive carbon (Super P), and 10% w/w poly(vinylidene difluoride) binder. The electrode with a 5:1:1 weight composition was also compared with the previously reported Li storage performance of HTO. The mixture was blended with a few drops of N-methyl-2-pyrrolidone (NMP, Sigma-Aldrich) to produce a gray-colored slurry. The slurries were cast on metal (Al or Cu) foils by doctor blading, and the resultant film was vacuum-dried at 120 °C for 12 h. After roller compression, film-type electrodes were cut into round discs with a geometric area of 1 cm². The loading amounts of the active materials

were 1.4−1.5 mg cm⁻². A 1.15 M $LiPF_6$ solution was dissolved in a 2:4:4 (v/v/v) ratio of ethylene carbonate/ethyl-methyl carbonate/dimethyl carbonate and adopted as an electrolyte. Galvanostatic charge/discharge analyses were performed using an automatic battery cycler (WBCS3000, WonaTech) at ambient temperature (30 °C). Electrochemical impedance spectroscopy (EIS) and cyclic voltammetry (CV) were conducted using a computer-controlled potentiostat (ZIVE SP2, WonaTech). EIS data were obtained at $E = 1.58$ V after 30 charge/discharge cycles. The frequency range was from 100 mHz to 100 kHz under AC stimulus with a 5 mV amplitude. The parameters of the equivalent circuit were calculated using ZMAN software.

Computational Details. Periodic DFT calculations were carried out using the Vienna ab initio simulation package (VASP).[16] We employed a generalized gradient approximation (GGA) parametrized by the Perdew−Burke−Ernzerhof (PBE) exchange−correlation functional.[17] Ionic cores were described using the projector augmented wave (PAW) method.[18] The wave functions were constructed from the expansion of planewaves with an energy cutoff of 520 eV. A 3 × 3 × 3 Monkhorst−Pack k-point mesh was used to sample the Brillouin zone. All calculations were converged until the forces on all atoms were less than 0.05 eV Å⁻¹. The electronic optimization steps were converged self-consistently to <10⁻⁶ eV. DFT+U within Dudarev's approach was used, $U_{eff} = 4.2$, to account for the on-site Coulomb interaction in the localized d orbital.[19] This U value was obtained by fitting the experimental data to the split between the occupied and unoccupied Ti d states for oxygen vacancy states at the (110) surface of the TiO_2[20] and has been used to model oxygen vacancies on other TiO_2 surfaces,[21] Nb and Ta substitution,[22] and the oxygen vacancy and Ti interstitial formation in TiO_2.[23] The transition state was located using the climbing image-nudged elastic band (CI-NEB) method.[24,25] Nine spaced images were obtained by linear interpolation and used as initial trajectories for the migration path. In the CI-NEB calculations, the images were refined until the maximum atomic forces converged to within 0.1 eV Å⁻¹. The difference in charge densities during Li migration was calculated using the following equation: $\Delta\rho = \rho LiTiO - (\rho TiO + \rho Li)$ where $\rho LiTiO$ is the total charge density of the LiTiO system, and ρTiO and ρLi are the charge densities of the TiO systems without Li and isolated Li atoms.[26,27]

■ RESULTS AND DISCUSSION

To use an in-depth kinetic study of Li to accurately explain the limitations associated with the electrochemical properties of
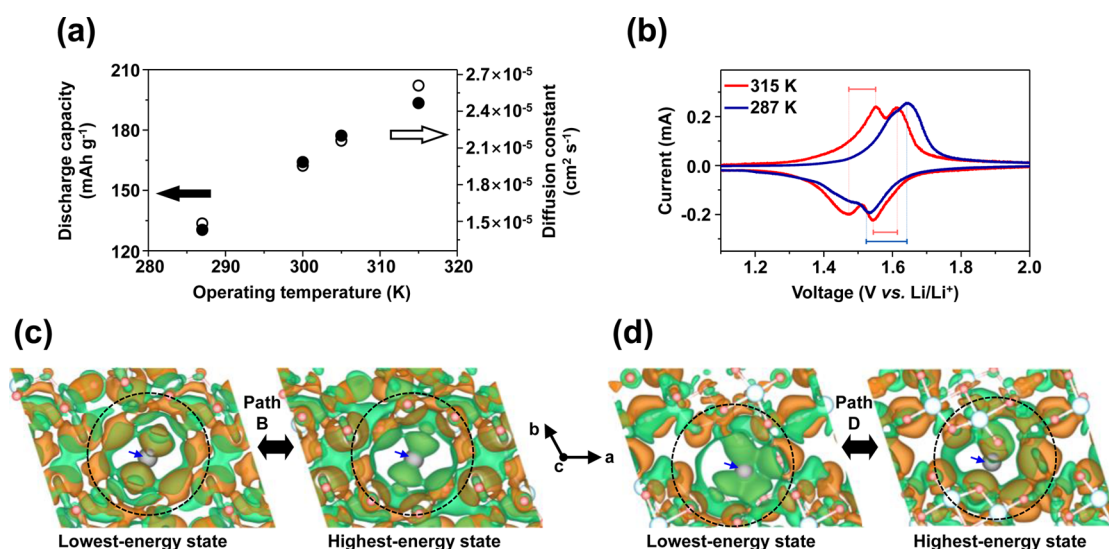
Figure 2. (a) Discharge capacities and diffusion constants of μ-HTO as a function of operating temperature. The diffusion constants were determined using the results of the DFT calculations based on Li migration through path B—the most favorable Li pathway. (b) CV curves for the μ-HTO (measured at 0.05 mV s^{-1}) at operating temperatures of 287 and 315 K. The polarization ranges of the potential are denoted. The evolution of differential charge densities inside the HTO crystal during Li migration through (c) path B and (d) path D. The left image was captured at stable positions, and the right image corresponds to the saddle point with the highest energy level along each Li migration pathway. The brown color indicates a gain of electrons, while the green color shows a loss of electrons. The isosurface levels of all images are 0.1 me Bohr^{-3}. The dotted circles indicate the Li interstitials, and the blue arrows point toward incorporated Li atoms.

HTO, it is necessary to quantitatively identify the motion of Li inside an HTO crystal and verify the existence of a close dependence between the Li storage performance and the movement of Li. A monoclinic $Na_2Ti_{12}O_{25}$ crystal model with a $P12/ma$ space group (ICSD ID: 28339) was utilized for the construction of the $H_2Ti_{12}O_{25}$ crystal model. After the Na of the $Na_2Ti_{12}O_{25}$ model was replaced with H, we performed DFT calculations to optimize the HTO crystal structure (see Computational Details). The hydrogen atoms in the HTO crystal exist in the form of a hydroxyl group, and the lengths of the O–H bonds are a consistent 98.4 pm.[28] The optimized structure and coordinates are presented in Figure S3.

There are four feasible pathways for the migration of Li inside the crystal: two paths along the a-axis and two paths along the c-axis (Figure S4). We tracked the evolution of energetics for each path and extracted the energy barriers to Li migration using DFT calculations and the CI-NEB method. Figure 1 shows the relative energies as a function of the movement of Li along a straight line projected between the two sites for each path. The calculated energy barriers for the paths B and D are 0.157 and 0.271 eV, respectively. The values of the energy barriers for the Li migration through paths A and C are 2.7–6.7-times higher than those for paths B and D. Therefore, there is severe anisotropy of the Li diffusion pathway inside the HTO, which indicates that the majority of Li migration occurs via penetrating tetragonal channels (paths B and D) in parallel with the c-axis.

In principle, the diffusion of Li is accelerated by increasing the ambient temperature, as described by the Arrhenius equation. Therefore, if the insertion/extraction of Li in HTO is a diffusion-controlled reaction, then the Li storage behavior of HTO should change significantly in response to variations in the temperature. We investigated the effect of operating temperature to verify the dependence of Li storage performance on the diffusivity of Li. The evolution of discharge capacities was monitored at various operating temperatures

ranging from 287–315 K. As a result, a large difference, 63 mAh g^{-1}, in the capacity was found when the operating temperature was increased from 287–315 K (Figure 2a). Consequently, the proportional relationship between the diffusion constant and the capacity verifies the dependence of the electrochemical performance of HTO materials on the kinetics of Li migration inside the crystal structure. A comparison between the capacities of LTO and HTO in response to temperature change also provides evidence for the diffusion-controlled Li insertion/extraction process of HTO (Figure S5).

The diffusion constant of Li can be estimated using the Einstein–Smoluchowski relationship as follows:

$$D = g\Gamma d^2 \tag{1}$$

where g ($\cong 1$) is a geometric factor, Γ ($v^* \exp - E_{act}/(k_BT)$) is the hopping frequency between sites ($v^* \cong 10^{13}$ Hz), and d is the migration distance.[29,30] The values of D for paths B and D ranged from 10^{-7}–10^{-4} cm^2 s^{-1} at a temperature of 305 K.[31] Table S1 shows detailed information on the determined diffusion characteristics.

Because of the effect of temperature, a decreased capacity as well as a larger level of polarization was observed at lower ambient temperatures. This is because the diffusion of Li become sluggish. The poor diffusion into HTO obstructs the movement of Li toward thermodynamically favorable insertion sites, which results in an increased internal resistance and a blockage of further lithiations. A comparison of the CV curves in Figure 2, panel b clearly shows that the polarization range of potential is remarkably larger when the HTO electrode is charged/discharged at low temperature.

As mentioned above, Li diffuses into HTO in a highly anisotropic manner via one-dimensional channels (paths B and D) developed in parallel with the c-axis. Also, comparing paths B and D shows that the Li diffusivity was higher in path B. As shown in Figure 2, panel b, the voltage plateau at 1.5 V is
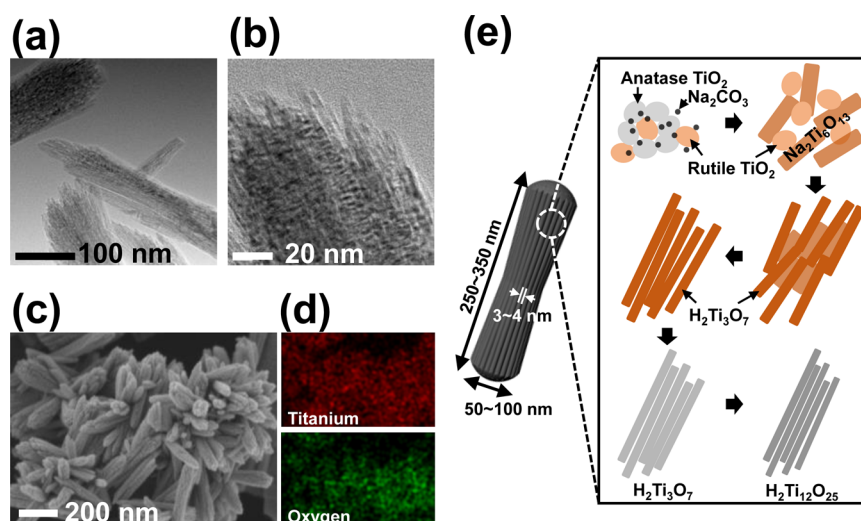
Figure 3. (a, b) TEM images of n-HTO crystals made from P 25 with anatase/rutile mixed phases. (c) SEM image of the n-HTO and (d) EDS element mapping results. (e) Schematic illustrations showing the formation of n-HTO driven by the kinetic gap of phase transformation between anatase and rutile TiO_2.

substantially attenuated at a low temperature of 287 K, while the plateau with a center at 1.58 V is relatively well preserved. The reason for this result lies in the kinetic discrepancy of Li diffusion along paths B and D. When a Li atom is incorporated at the interstitial sites of the HTO crystal, Li modifies the distribution of charge traps within HTO. The electronic charges are distributed over Ti atoms adjacent to Li interstitials, which results in binding between the Li and the trapped electrons. During the collective migration of Li and electrons inside HTO, the atomic geometry and crystallographic direction along the migration path have a significant effect on the energy barrier and on site-to-site Li mobility.[32,33] In the middle of path B, the Li atoms are surrounded by orthorhombic Ti lattices, regardless of the stable (lowest energy) or saddle (highest energy) points. The Li atoms constantly maintain the binding that is developed along the [110] direction, and as a consequence, slight energy variation/diffusion barriers are generated for path B migration (Figure 2c). By contrast, at the stable point of path D, Li is surrounded by three point-sharing octahedral Ti sites, which results in an extraordinarily stable energy state and a higher energy barrier for path D (Figure 2d). For this reason, the relatively sluggish Li mobility makes it difficult to access the Li insertion sites through path D at a lower temperature of 287 K. Therefore, it can be concluded that the voltage plateaus at 1.5 and 1.58 V indicate Li insertion through paths D and B, respectively.

The strong dependence of Li storage performance on its diffusivity explains the limited rate capability and continued capacity fading of micrometer-sized bulky HTO (referred to as μ-HTO). In our close investigations, μ-HTO shows a capacity retention of 41% at a high current density of 1 A g^{-1} and a capacity fading of 34% during 300 charge/discharge measurements (see Figure S6 and a detailed description in the Supporting Information). Also, this Li storage performance of μ-HTO is consistent with that of the HTO reported in the literature (Figure S7).[15] It should be noted that the μ-HTO electrodes with HTO/conductive carbon/binder weight ratios of 5:1:1 deliver a discharge capacity of 240 mAh g^{-1}, which agrees with values found in the literature. All HTO electrodes fabricated in this study were based on a weight ratio of 8:1:1.

An understanding of Li dynamics and the effect on Li storage performance convinced us to develop a nanostructured HTO. The time constant, t, for Li diffusion ($t = L^2/D$) is an important factor that is responsible for the limited power or rate capability of an electrode material. Thus, in attempts to reduce the Li transfer length (L) and minimize resistive behavior, a nanostructured HTO with the shape of a nanobundle (referred to as n-HTO) was synthesized. It should be noted that the crystal structure of the starting TiO_2 materials is highly important and determines the shape and size of the HTO products.

Figure 3, panels a−c show the TEM and SEM images of n-HTO with a bundle-structure containing HTO nanorods. Each single nanorod has a diameter of 3−4 nm, and the entire n-HTO bundle has a diameter of 50−100 nm and a length of 250−350 nm (Figure 3e). Energy dispersive spectrometry (EDS) element mapping results (Figure 3d) prove that the n-HTO is composed of mainly elemental Ti and O and that impurities such as elemental Na and C are essentially absent. Considering the diffusion length ($\geq$ half of 4 nm) inside the HTO nanorods, the minimum diffusion times (at 305 K) of paths B and D correspond to 1.9 and 77 ns, respectively, which indicates that the kinetics of the lithiation/delithiation reaction in n-HTO is three orders of magnitude faster than that in μ-HTO.

For the synthesis of n-HTO, we focused on the initial synthetic step from TiO_2 to $Na_2Ti_3O_7$ during the solid-state HTO synthesis (Figure S2). This recrystallization of TiO_2 to produce $Na_2Ti_3O_7$ is particularly noteworthy because it involves drastic structural changes in the atomic and nanoscales (Figure S8). During the synthesis, the crystalline phases of the reactants are highly important because TiO_2 particles with different crystal structures and phase stabilities cause different reaction rates and pathways. If the TiO_2 particles containing both anatase and rutile phases were utilized for the synthesis of $Na_2Ti_3O_7$, the differences in the rate, namely a "kinetic gap" of structural transformation, can be induced by virtue of varied thermal stabilities. It is well-known that rutile forms show higher phase stabilities than anatase forms at all temperatures.[34,35]
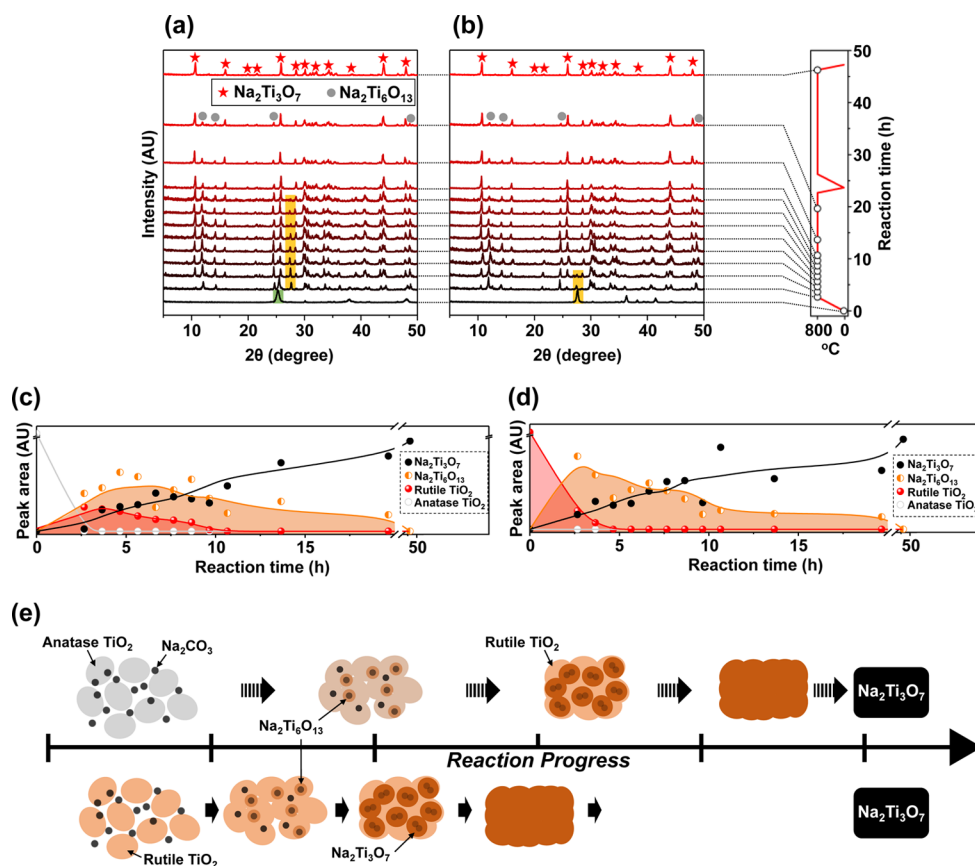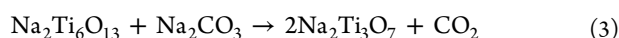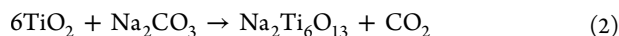
Figure 4. Evolution of the XRD pattern during phase transformation. (a) Anatase TiO_2 → $Na_2Ti_3O_7$ and (b) rutile TiO_2 → $Na_2Ti_3O_7$. The XRD peaks corresponding to anatase and rutile TiO_2 phases are indicated by green and yellow shadows, respectively. (c, d) The XRD peak areas of reactants (anatase or rutile TiO_2), intermediate ($Na_2Ti_6O_{13}$), and product ($Na_2Ti_3O_7$) as a function of reaction time. The peak areas of anatase TiO_2, rutile TiO_2, $Na_2Ti_6O_{13}$, and $Na_2Ti_3O_7$ were obtained from major XRD peaks located at 25.28°, 27.51°, 11.84°, and 10.56°. (e) Schematic illustrations showing the kinetic gap during the TiO_2 → $Na_2Ti_3O_7$ phase transformations when anatase and rutile TiO_2 were adopted as starting materials, respectively.

To identify the kinetic gap during the structural transformation from TiO_2 to $Na_2Ti_3O_7$, we conducted time-resolved XRD measurements for both anatase and rutile TiO_2. A mixture of TiO_2 (anatase or rutile) and Na_2CO_3 powders was heat-treated (24 h × 2 at 800 °C) under air for XRD measurement. Figure 4, panels a and c display the evolution of the XRD pattern and the corresponding peak areas as a function of time when pure anatase TiO_2 particles were used as a starting material. Figure 4, panels b and d are the same as those above, with the exception that pure rutile TiO_2 particles were used. Before the temperature had risen, the XRD patterns for anatase (JCPDS No. 01−0562) and rutile (JCPDS No. 02−0494)-phased TiO_2 both exactly matched with references. The overall structural transformation consists of a multistep reaction of TiO_2 → $Na_2Ti_6O_{13}$ (JCPDS No. 14−0277) → $Na_2Ti_3O_7$ (JCPDS No. 14−0085), as follows:

$$6TiO_2 + Na_2CO_3 \rightarrow Na_2Ti_6O_{13} + CO_2 \qquad (2)$$

$$Na_2Ti_6O_{13} + Na_2CO_3 \rightarrow 2Na_2Ti_3O_7 + CO_2 \qquad (3)$$

where the $Na_2Ti_6O_{13}$ is a transient species within this multistep reaction.

A comparison of the phase evolution of the material indicates that there is a kinetic gap in the structural transformations between anatase and rutile TiO_2 (Figure 4c,d). Upon heat treatment, the anatase TiO_2, which has a relatively lower thermal stability, is first converted to rutile TiO_2 within 2 h, and

the peaks for the $Na_2Ti_6O_{13}$ intermediate then begin to appear. After 7 h of reaction, the contents of $Na_2Ti_6O_{13}$ gradually decrease to form $Na_2Ti_3O_7$. In this situation, the rutile TiO_2 derived from anatase completely disappears after 10 h of reaction time. On the other hand, the rutile form of TiO_2 instantly participates in the reaction to form $Na_2Ti_6O_{13}$. Most of the TiO_2 species disappears within 5 h, and the $Na_2Ti_6O_{13}$ also begins to fade after 3 h. On the basis of the fact that the TiO_2 species is completely consumed, there is a time lag of 7 h between anatase and rutile TiO_2, which generates the kinetic gap that is associated with the structural transformation (Figure 4e).

As it turns out, the presence of a kinetic gap during the structural transformation was applied to create the nanostructured HTO. First, TiO_2 particles with anatase/rutile mixed phases were employed for the synthesis of HTO. It is well-known that Aeroxide P25 TiO_2 particles made by Evonik (referred to as P25) are composed of mixtures of anatase and rutile crystallites with a reported ratio of approximately 70:30.[36] The coexistence of anatase and rutile phases and the difference in the speed of the structural transformation segregate the locations where the reaction occurs. As schematically shown in Figure 3, panel e, the rutile phase constituting P 25 reacts rapidly with Na_2CO_3 to generate sodium titanate compounds ($Na_2Ti_6O_{13}$ and subsequent $Na_2Ti_3O_7$) in the shape of nanorods. Concurrently, the anatase phases promote a

preferential transformation into rutile phases. The rutile phases originating from the anatase portions later react with Na_2CO_3, which was already under way for the intrinsic rutile. As a result, nanobundle shaped nanostructured n-HTO can be obtained. No noticeable nanostructural changes were observed in the following dehydration ($4H_2Ti_3O_7 \rightarrow H_2Ti_{12}O_{25} + 3H_2O$) upon heating at 260 °C (Figure S9).

As discussed above, our main objective was to produce n-HTO with a reduced resistive behavior stemming from the sluggish Li diffusion inside the HTO crystal. Figure 5, panel a
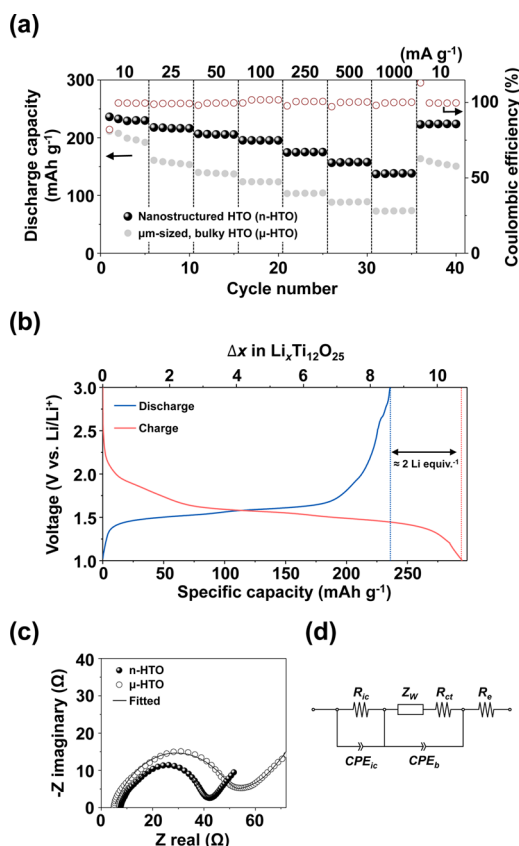

(a)

(b)

(c)   **(d)**

Figure 5. (a) Specific capacities of HTO electrodes measured at various current densities. The Coulombic efficiencies of n-HTO are denoted. (b) First charge/discharge voltage profile of n-HTO at 10 mA g^{-1}. (c) Nyquist plots obtained from electrodes composed of n-HTO and μ-HTO. (d) Equivalent circuit model for fitting.

shows the discharge capacities of the n-HTO obtained at various current densities (10−1000 mA g^{-1}). The electrode composed of n-HTO stably delivers reversible capacities of 230, 216, 206, 195, 175, 158, and 138 mAh g^{-1} with an almost 100% Coulombic efficiency at current densities of 10, 25, 50, 100, 250, 500, and 1000 mA g^{-1}, respectively (Figure S10). The rate capability of the n-HTO is significantly better than the values for bulky μ-HTOs. The observed maximum capacity of the n-HTO exceeds the theoretical capacity of LTO (175 mAh g^{-1}). In addition, the n-HTO shows a long duration of cyclic stability with no significant capacity fading (Figure S11).

The highly conductive state signifies that the electrochemical characteristics of n-HTO represent the thermodynamic properties of the materials. Therefore, the detailed mechanism of the Li insertion/extraction process can be understood via electrochemical analyses. The data in Figure 5, panel b show the charge/discharge voltage profile at the first cycle. During the

first lithiation process, n-HTO accepts about 10.7 Li equiv^{-1}, which correspond to a specific capacity of 295 mAh g^{-1}. Also, approximately 8.6 Li equiv^{-1} (236 mAh g^{-1}) are released in subsequent delithiations. It should be noted that about 2 Li equiv^{-1} are irreversibly inserted inside the HTO crystal. This phenomenon can be explained by the fact that the 2 Li$^+$ ions substitute pre-existing H$^+$ ions of HTO. Before the insertion of Li, the H$^+$ ions maintain the charge balance of the HTO crystal in which Ti atoms show Ti^{4+} states. The incorporation of Li during the first lithiation induces switching from H$^+$ to Li$^+$, which explains the exceptionally high specific capacity of HTO (or $Li_2Ti_{12}O_{25}$). After the first lithiation, the capacity corresponding to 2 Li equiv^{-1} is not recovered, and, consequently, about 8.7 Li equiv^{-1} are reversibly inserted/extracted ($Li_2Ti_{12}O_{25} \leftrightarrow Li_{10.7}Ti_{12}O_{25}$).

We performed EIS analyses to quantitatively determine the differences in electron/mass transfer resistance between n-HTO and μ-HTO. Figure 5, panels c and d show the Nyquist plots obtained after 30 charge/discharge cycles and an equivalent circuit model for the fitting of the EIS results.[6,37] On the basis of the fitting results, we extracted each kinetic parameter from the experimental data (Table 1). Among the

Table 1. Fitting Parameters Used To Simulate the EIS Data

parameter	unit	active material	
		n-HTO	μ-HTO
R_e	Ω	7.51	4.98
R_{ct}	Ω	32.7	48.1
R_{ic}	Ω	1.58	9.23
$A_W{}^a$	mΩ s$^{-0.5}$	0.017	0.016

^{a}The Warburg coefficient is determined as follows:

$$A_W = \frac{RT}{An^2F^2\theta C\sqrt{2D}}$$

where R is the gas constant, T is the temperature, A is the diffusion area, n is the valency, F is the Faraday constant, C is the concentration of Li$^+$, D is the diffusion coefficient of Li in the electrode, and θ denotes the fraction of the reduced and oxidized species present.

kinetic parameters, R_e corresponds to an equivalent series resistance, and CPEs are constant-phase elements. Z_W is the Warburg element related to the diffusion of Li inside the crystal. Since the Warburg coefficient (A_W), which is directly converted to the diffusion coefficient, is an intrinsic property of HTO crystals, the values of A_W for both n-HTO and μ-HTO are in a similar range. The value of R_{ct}, electrolyte/HTO charge transfer resistance, of n-HTO (32.7 Ω) is smaller than that of μ-HTO (48.1 Ω), which confirms the superior mass conductance inside the n-HTO electrode material. Interestingly, the value of R_{ic}, charge transfer resistance between intercrystallites, corresponding to n-HTO (1.58 Ω) is significantly smaller than that of μ-HTO (9.23 Ω). This result indicates that the unique nanostructure of n-HTO not only improves the kinetics of Li diffusion, but also assures a low electronic contact resistance between individual HTO particles because a closely packed bundle of HTO nanorods facilitates the delivery of electrons across primary crystallites. Consequently, on the basis of the EIS data, the bundled structure of n-HTO relieves the resistive behavior, which explains the superior rate capability of this material.

CONCLUSIONS

Nanostructured HTO particles and their facilitated Li diffusion dynamics were proposed as advanced high voltage anode materials in this study. We first investigated the Li diffusion pathways and kinetics that account for a significant portion of the Li storage performance of HTO. Coupled with DFT calculations, two paths were proposed as feasible routes for Li diffusion, and these paths play major roles in the anisotropic (de)lithiation process of HTO. In addition, to solve the problematic rate capability and cyclic stability of conventional μ-HTO, a n-HTO with the shape of nanobundles was synthesized utilizing a kinetic gap during the structural transformation of different phases of TiO_2. The synthesized n-HTO exhibited a superior power performance compared with its micrometer-sized counterpart. The Li storage performance and facile synthetic process of the nanostructured HTO reported herein indicate that it deserves to be considered as a promising high-voltage anode material for the construction of safe LIBs.

ASSOCIATED CONTENT

Ⓢ Supporting Information

The Supporting Information is available free of charge on the ACS Publications website at DOI: 10.1021/acsami.6b02842.

> Detailed results of electrochemical measurements (voltage profiles, long cycle test); DFT-optimized crystal structure of HTO and its Cartesian coordinates; diffusion characteristics of Li inside the HTO crystal; TEM images of samples (PDF)

AUTHOR INFORMATION

Corresponding Author
*E-mail: jyi@snu.ac.kr. Phone: +82-2-880-7438.

Author Contributions
§These authors contributed equally to this work. The manuscript was written through contributions of all authors. All authors have given approval to the final version of the manuscript.

Notes
The authors declare no competing financial interest.

ACKNOWLEDGMENTS

REFERENCES

(1) Soloveichik, G. L. Battery Technnologies for Large-Scale Stationary Energy Storage. *Annu. Rev. Chem. Biomol. Eng.* **2011**, *2*, 503−527.

(2) Dunn, B.; Kamath, H.; Tarascon, J. − M. Electrical Energy Storage for the Grid: A Battery of Choices. *Science* **2011**, *334*, 928−935.

(3) Yi, T. − F.; Yang, S. − Y.; Xie, Y. Recent Advances of $Li_4Ti_5O_{12}$ as a Promising Next Generation Anode Material for High Power Lithium-Ion Batteries. *J. Mater. Chem. A* **2015**, *3*, 5750−5777.

(4) Dylla, A. G.; Henkelman, G.; Stevenson, K. J. Lithium Insertion in Nanostructured TiO_2 (B) Architectures. *Acc. Chem. Res.* **2013**, *46*, 1104−1112.

(5) Lee, E. J.; Nam, I.; Yi, J.; Bang, J. H. Nanoporous Hexagonal TiO_2 Superstructure as a Multifunctional Material for Energy Conversion and Storage. *J. Mater. Chem. A* **2015**, *3*, 3500−3510.

(6) Baek, J.; Park, S.; Song, C. K.; Kim, T. Y.; Nam, I.; Lee, J. M.; Han, J. W.; Yi, J. Radial Alignment of c-Channel Nanorods in 3D Porous TiO_2 for Eliciting Enhanced Li Storage Performance. *Chem. Commun.* **2015**, *51*, 15019−15022.

(7) Sun, X.; Radovanovic, P. V.; Cui, B. Advances in Spinel $Li_4Ti_5O_{12}$ Anode Materials for Lithium-Ion Batteries. *New J. Chem.* **2015**, *39*, 38−63.

(8) Song, T.; Paik, U. TiO_2 as an Active or Supplemental Material for Lithium Batteries. *J. Mater. Chem. A* **2016**, *4*, 14−31.

(9) Ren, Y.; Liu, Z.; Pourpoint, F.; Armstrong, A. R.; Grey, C. P.; Bruce, P. G. Nanoparticulate TiO_2(B): An Anode for Lithium-Ion Batteries. *Angew. Chem.* **2012**, *124*, 2206−2209.

(10) Liu, S.; Jia, H.; Han, L.; Wang, J.; Gao, P.; Xu, D.; Yang, J.; Che, S. Nanosheet-Constructed Porous TiO_2-B for Advanced Lithium Ion Batteries. *Adv. Mater.* **2012**, *24*, 3201−3204.

(11) Chen, C.; Hu, X.; Wang, Z.; Xiong, X.; Hu, P.; Liu, Y.; Huang, Y. Controllable Growth of TiO_2-B Nanosheet Arrays on Carbon Nanotubes as a High-Rate Anode Material for Lithium-Ion Batteries. *Carbon* **2014**, *69*, 302−310.

(12) Chen, C.; Hu, X.; Zhang, B.; Miao, L.; Huang, Y. Architectural Design and Phase Engineering of N/B-Codoped TiO_2(B)/Anatase Nanotube Assemblies for High-Rate and Long-Life Lithium Storage. *J. Mater. Chem. A* **2015**, *3*, 22591−22598.

(13) Morgado, E., Jr.; Jardim, P. M.; Marinkovic, B. A.; Rizzo, F. C.; de Abreu, M. A. S.; Zotin, J. L.; Araújo, A. S. Multistep Structural Transition of Hydrogen Trititanate Nanotubes into TiO_2-B Nanotubes: A Comparison Study Between Nanostructured and Bulk Materials. *Nanotechnology* **2007**, *18*, 495710.

(14) Akimoto, J.; Chiba, K.; Kijima, N.; Hayakawa, H.; Hayashi, S.; Gotoh, Y.; Idemoto, Y. Soft-Chemical Synthesis and Electrochemical Property of $H_2Ti_{12}O_{25}$ as a Negative Electrode Material for Rechargeable Lithium-Ion Batteries. *J. Electrochem. Soc.* **2011**, *158*, A546−A549.

(15) Akimoto, J.; Kataoka, K.; Kojima, N.; Hayashi, S.; Gotoh, Y.; Sotokawa, T.; Kumashiro, Y. A Novel Soft-Chemical Synthetic Route Using $Na_2Ti_6O_{13}$ as a Starting Compound and Electrochemical Properties of $H_2Ti_{12}O_{25}$. *J. Power Sources* **2013**, *244*, 679−683.

(16) Kresse, G.; Furthmüller, J. Efficient Iterative Schemes for *Ab Initio* Total-Energy Calculations Using a Plane-Wave Basis Set. *Phys. Rev. B: Condens. Matter Mater. Phys.* **1996**, *54*, 11169−11186.

(17) Perdew, J. P.; Burke, K.; Ernzerhof, M. Generalized Gradient Approximation Made Simple. *Phys. Rev. Lett.* **1996**, *77*, 3865−3868.

(18) Blöchl, P. E. Projector Augmented-Wave Method. *Phys. Rev. B: Condens. Matter Mater. Phys.* **1994**, *50*, 17953−17979.

(19) Dudarev, S. L.; Botton, G. A.; Savrasov, S. Y.; Humphreys, C. J.; Sutton, A. P. Electron-Energy-Loss Spectra and the Structural Stability of Nickel Oxide: An LSDA+U Study. *Phys. Rev. B: Condens. Matter Mater. Phys.* **1998**, *57*, 1505−1509.

(20) Morgan, B. J.; Watson, G. W. A DFT+*U* Description of Oxygen Vacancies at the TiO_2 Rutile (110) Surface. *Surf. Sci.* **2007**, *601*, 5034−5041.

(21) Morgan, B. J.; Watson, G. W. A Density Functional Theory+*U* Study of Oxygen Vacancy Formation at the (110), (100), (101), and (001) Surfaces of Rutile TiO_2. *J. Phys. Chem. C* **2009**, *113*, 7322−7328.

(22) Morgan, B. J.; Scanlon, D. O.; Watson, G. W. Small Polarons in Nb- and Ta-Doped Rutile and Anatase TiO_2. *J. Mater. Chem.* **2009**, *19*, 5175−5178.

(23) Morgan, B. J.; Watson, G. W. Intrinsic n-Type Defect Formation in TiO_2: A Comparison of Rutile and Anatase from GGA+*U* Calculations. *J. Phys. Chem. C* **2010**, *114*, 2321−2328.

(24) Henkelman, G.; Uberuaga, B. P.; Jónsson, H. A Climbing Image Nudged Elastic Band Method for Finding Saddle Points and Minimum Energy Paths. *J. Chem. Phys.* **2000**, *113*, 9901−9904.

(25) Henkelman, G.; Jónsson, H. Improved Tangent Estimate in the Nudged Elastic Band Method for Finding Minimum Energy Paths and Saddle Points. *J. Chem. Phys.* **2000**, *113*, 9978−9985.

(26) Yun, Y. S.; Lee, K. R.; Park, H.; Kim, T. Y.; Yun, D.; Han, J. W.; Yi, J. Rational Design of a Bifunctional Catalyst for the Oxydehydration of Glycerol: A Combined Theoretical and Experimental Study. *ACS Catal.* **2015**, *5*, 82−94.

(27) Kang, J.; Hirata, A.; Kang, L.; Zhang, X.; Hou, Y.; Chen, L.; Li, C.; Fujita, T.; Akagi, K.; Chen, M. Enhanced Supercapacitor Performance of MnO_2 by Atomic Doping. *Angew. Chem., Int. Ed.* **2013**, *52*, 1664−1667.

(28) Chen, H.-Y. T.; Tosoni, S.; Pacchioni, G. Hydrogen Adsorption, Dissociation, and Spillover on Ru_{10} Clusters Supported on Anatase TiO_2 and Tetragonal ZrO_2 (101) Surfaces. *ACS Catal.* **2015**, *5*, 5486−5495.

(29) Kang, K.; Morgan, D.; Ceder, G. First Principles Study of Li Diffusion in I-Li_2NiO_2 Structure. *Phys. Rev. B: Condens. Matter Mater. Phys.* **2009**, *79*, 014305.

(30) Ning, F.; Li, S.; Xu, B.; Ouyang, C. Strain Tuned Li Diffusion in $LiCoO_2$ Material for Li Ion Batteries: A First Principles Study. *Solid State Ionics* **2014**, *263*, 46−48.

(31) Persson, K.; Sethuraman, V. A.; Hardwick, L. J.; Hinuma, Y.; Meng, Y. S.; van der Ven, A.; Srinivasan, V.; Kostecki, R.; Ceder, G. Lithium Diffusion in Graphitic Carbon. *J. Phys. Chem. Lett.* **2010**, *1*, 1176−1180.

(32) Yildirim, H.; Greeley, J. P.; Sankaranarayanan, S. K. R. S. The Effect of Concentration on Li Diffusivity and Conductivity in Rutile TiO_2. *Phys. Chem. Chem. Phys.* **2012**, *14*, 4565−4576.

(33) Yildirim, H.; Greeley, J.; Sankaranarayanan, S. K. R. S. Effect of Concentration on the Energetics and Dynamics of Li Ion Transport in Anatase and Amorphous TiO_2. *J. Phys. Chem. C* **2011**, *115*, 15661−15673.

(34) Hanaor, D. A. H.; Sorrell, C. C. Review of the Anatase to Rutile Phase Transformation. *J. Mater. Sci.* **2011**, *46*, 855−874.

(35) Muscat, J.; Swamy, V.; Harrison, N. M. First-Principles Calculations of the Phase Stability of TiO_2. *Phys. Rev. B: Condens. Matter Mater. Phys.* **2002**, *65*, 224112.

(36) Hurum, D. C.; Agrios, A. G.; Gray, K. A.; Rajh, T.; Thurnauer, M. C. Explaining the Enhanced Photocatalytic Activity of Degussa P25 Mixed-Phase TiO_2 Using EPR. *J. Phys. Chem. B* **2003**, *107*, 4545−4549.

(37) Xin, L.; Liu, Y.; Li, B.; Zhou, X.; Shen, H.; Zhao, W.; Liang, C. Constructing Hierarchical Submicrotubes from Interconnected TiO_2 Nanocrystals for High Reversible Capacity and Long-Life Lithium-Ion Batteries. *Sci. Rep.* **2014**, *4*, 4479.